AFRL-AFOSR-VA-TR-2022-0001

Reaction-Induced Sintering for Fabrication of Bulk Nanoporous and Composite Metals

McDowell, Matthew
GEORGIA TECH RESEARCH CORPORATION
926 DALNEY ST NW
ATLANTA, GA, 30332
USA

10/04/2021
Final Technical Report

Air Force Research Laboratory
Air Force Office of Scientific Research
Arlington, Virginia 22203
Air Force Materiel Command

REPORT DOCUMENTATION PAGE

Form Approved
OMB No. 0704-0188

1. REPORT DATE *(DD-MM-YYYY)*	**2. REPORT TYPE**	**3. DATES COVERED** *(From - To)*
04-10-2021	Final	01 Apr 2017 - 31 Mar 2020

4. TITLE AND SUBTITLE
Reaction-Induced Sintering for Fabrication of Bulk Nanoporous and Composite Metals

5a. CONTRACT NUMBER

5b. GRANT NUMBER
FA9550-17-1-0130

5c. PROGRAM ELEMENT NUMBER
61102F

6. AUTHOR(S)
Matthew McDowell

5d. PROJECT NUMBER

5e. TASK NUMBER

5f. WORK UNIT NUMBER

7. PERFORMING ORGANIZATION NAME(S) AND ADDRESS(ES)
GEORGIA TECH RESEARCH CORPORATION
926 DALNEY ST NW
ATLANTA, GA 30332
USA

8. PERFORMING ORGANIZATION REPORT NUMBER

9. SPONSORING/MONITORING AGENCY NAME(S) AND ADDRESS(ES)
AF Office of Scientific Research
875 N. Randolph St. Room 3112
Arlington, VA 22203

10. SPONSOR/MONITOR'S ACRONYM(S)
AFRL/AFOSR RTA1

11. SPONSOR/MONITOR'S REPORT NUMBER(S)
AFRL-AFOSR-VA-TR-2022-0001

12. DISTRIBUTION/AVAILABILITY STATEMENT
A Distribution Unlimited: PB Public Release

13. SUPPLEMENTARY NOTES

14. ABSTRACT
Over the course of this project, we have accomplished the following, which all fall under the theme of understanding alloying processes in lithium metal alloys:
1. Discovered and investigated spontaneous nanowire and microwire growth from the surface of Li-rich lithium-metal alloys
2. Developed new procedures for creating lightweight metals with tunable porosity via chemical lithium dealloying procedures, taking advantage of reaction-induced sintering
3. Investigated the synthesized porous metal monoliths for their energy storage properties
4. Constructed uniaxial pressure cells to measure stress changes in metals within solid-state batteries
This section details each of these accomplishments.

15. SUBJECT TERMS

16. SECURITY CLASSIFICATION OF:			**17. LIMITATION OF ABSTRACT**	**18. NUMBER OF PAGES**	**19a. NAME OF RESPONSIBLE PERSON**
a. REPORT	**b. ABSTRACT**	**c. THIS PAGE**			MING-JEN PAN
U	U	U	UU	19	**19b. TELEPHONE NUMBER** *(Include area code)* 703-696-7343

Standard Form 298 (Rev.8/98)
Prescribed by ANSI Std. Z39.18

Final Performance Report

AFOSR Grant Number FA9550-17-1-0130

Project Title: “Reaction-Induced Sintering for Fabrication of Bulk Nanoporous and Composite Metals”

Principal Investigator: Prof. Matthew T. McDowell

Supported Ph.D. Student: Sang Yun Han

Institution: Georgia Tech Research Corporation

Program Officer: Ming-Jen Pan

Reporting Period: April 1, 2017 – December 31, 2020

I. Project Overview and Research Objectives

This research project is focused on enabling new processing routes for the fabrication of low-density nanostructured metals by taking advantage of the high chemical reactivity and diffusivity of alkali metals (in particular, lithium). The use of low-temperature lithium-based processing methods could enable entirely new nanostructured and nanoporous metals to be fabricated, since the low temperatures utilized (< 300 °C) can activate kinetically-controlled pathways during fabrication. This is important since conventional high-temperature processing methods are not suitable for the fabrication of bulk metal nanostructures; for instance, high-temperature sintering of metal nanoparticle arrays will cause grain growth and consolidation instead of direct fusion to form a nanocrystalline and/or nanoporous material. Dealloying of noble metals is an established processing route for the fabrication of nanoporous gold, but this technique is only suitable for a few precious metals and cannot produce structural materials such as aluminum or magnesium.[1] Thus, new low-temperature synthesis methodologies are necessary for the creation of a wide variety of nanostructured metals.

The overall objective of this research project is to develop and understand the nanoscale mechanisms for the synthesis of nanostructured materials when using lithium as a processing agent at low temperatures, and thereby enable new fabrication methods for nanostructured/low-density materials. An aspect of this is "reaction-induced sintering" (Fig. 1), which is the joining of Li-rich alloy particles due to diffusive reaction at interfaces. The desired outcome of this project is to gain the scientific understanding necessary to utilize alkali metal reactions as a bulk-scale processing technique to create nanoporous metals. The specific research objectives of this project are as follows:

1. Develop new lithium-based processing techniques and determine how various parameters influence the structure and properties of fabricated nanomaterials.
2. Uncover the dynamic nanoscale structural and chemical mechanisms underlying these fabrication processes.
3. Determine the deformation behavior and mechanical properties of such materials.

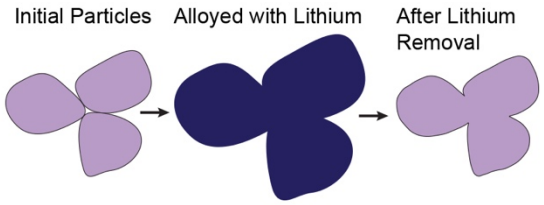

Figure 1. Schematic of reaction-induced sintering.

II. Status of Research Effort

This research project started on April 1, 2017, and this final report details the accomplishments throughout the overall effort t. One Ph.D. student (Sang Yun Han) was supported to perform the research. Funds for this project were expended according to the initial budget, with a large portion of the funds going to support the stipend and tuition of the Ph.D. student. A no-cost extension was received to perform the research for one additional year. The research outputs of this effort are as follows:

Publications:

1. J. A. Lewis, F. J. Q. Cortes, Y. Liu, J. C. Miers, A. Verma, B. S. Vishnugopi, J. Tippens, D. Prakash, T. S. Marchese, S. Y. Han, C. Lee, P. P. Shetty, H.-W. Lee, P. Shevchenko, F. De Carlo, C. Saldana, P. P. Mukherjee, M. T. McDowell "Linking Void and Interphase Evolution to Electrochemistry in Solid-State Batteries Using *Operando* X-Ray Tomography" *Nature Materials*, **2021**, DOI: 10.1038/s41563-020-00903-2.
2. S. Y. Han, J. A. Lewis, P. P. Shetty, J. Tippens, D. Yeh, T. S. Marchese, M. T. McDowell "Porous Metals from Chemical Dealloying for Solid-State Battery Anodes" *Chemistry of Materials,* **2020**, 32, (6), 2461-2469.
3. S. Y. Han, M. G. Boebinger, N. P. Kondekar, T. J. Worthy, M. T. McDowell "Seeded Nanowire and Microwire Growth from Lithium Alloys" *Nano Letters*, **2018**, 18, (7), 4331-4337.

Presentations:

1. M. T. McDowell, "Watching Batteries Work: Understanding Reaction Mechanisms in Next-Generation Battery Materials." Telluride Science Virtual Lecture Series (Virtual), June 2020.
2. S. Y. Han, M. G. Boebinger, D. Yeh, M. T. McDowell, "Scalable Porous Metals from Lithium Alloys." 236th Electrochemical Society Meeting, Atlanta, GA, October 2019.
3. S. Y. Han, M. T. McDowell, "Seeded Nanowire Growth from Lithium Alloys." Materials Research Society 2018 Fall Meeting, Boston, MA, November 2018.
4. M. T. McDowell, "In Situ Investigation of the Dynamic Evolution of Materials and Interfaces in Batteries." Telluride Science Research Center Workshop, Telluride, CO, July 2018.

III. Research Accomplishments

Over the course of this project, we have accomplished the following, which all fall under the theme of understanding alloying processes in lithium metal alloys:

1. Discovered and investigated spontaneous nanowire and microwire growth from the surface of Li-rich lithium-metal alloys
2. Developed new procedures for creating lightweight metals with tunable porosity via chemical lithium dealloying procedures, taking advantage of reaction-induced sintering
3. Investigated the synthesized porous metal monoliths for their energy storage properties
4. Constructed uniaxial pressure cells to measure stress changes in metals within solid-state batteries

This section details each of these accomplishments.

IIIa. Nano- and microwire growth from lithium/metal alloys

Although vapor-liquid-solid (VLS) growth of nanowires from alloy seed particles is common in various semiconductor systems, related wire growth in all-metal systems is rare. As part of this project, we discovered and fundamentally investigated the spontaneous growth of nano- and microwires from metal seed particles during the cooling of lithium-rich bulk alloys. This process is initiated by heating metal foil bilayers (lithium with gold, silver, or indium) at temperatures below 300 °C to form alloys, followed by cooling. The as-grown wires feature Au-, Ag-, or In-rich metal tips and LiOH shafts; the results strongly suggest that the wires grow as Li metal and are converted to polycrystalline LiOH during and/or after growth due to exposure to H_2O. This process is a simple and scalable way to create nanostructures over large areas, and the findings suggest that by controlling the O_2 and H_2O content in the surrounding atmosphere, metal nanowire growth from alloy seeds could be possible in a variety of systems. This could lead to new methods for creating nanoporous metals at the bulk scale.

Heating and cooling procedures of metal bilayers were found to induce wire growth. In these experiments, Au, Ag, or In foils were pressed onto Li foils and heated to temperatures above the melting point of Li (180.5 °C) for four hours on a hot plate in an argon-filled glove box, followed be cooling naturally. Li was controlled to be in excess (molar ratios of between 15 and 20 mol Li to 1 mol of the other metal were used in most experiments). After this procedure, the surfaces of the samples were found to be covered in nano- and microwires, as shown in Fig. 2. Figure 2a is an SEM image of wires grown from a Li-Au sample. The wires are straight with uniform diameter, and the wire tips exhibit brighter contrast; this is reminiscent of Si nanowires grown from Au catalysts.[2] Figure 2b shows a low-magnification SEM image of the Li-Au sample after cooling; wires are observed to cover the entire surface. Figure 2c is an intermediate-magnification view of the wires grown from Li-Au. Figure 2d and e show similar wires grown

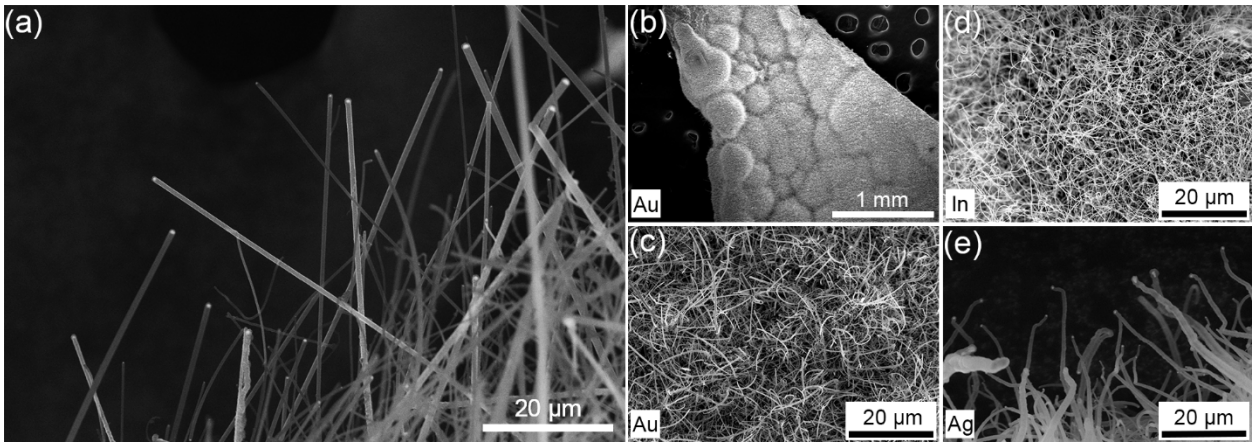

Figure 2. SEM images of wires grown from Li alloys. **(a)** Wires grown from a Li-Au alloy (a Li:Au molar ratio of 20:1 was used). **(b)** A low-magnification view of a Li-Au sample covered with wires. **(c)** Intermediate-magnification image of Li-Au wires. **(d)** Wires growth from a Li-In sample with a molar ratio of 20:1. **(e)** Wires grown from a Li-Ag sample (15:1 molar ratio).

from Li-Ag and Li-In samples heated and cooled in the same manner. These wires appear similar to the wires from the Li-Au sample, except that the wires from the Li-Ag sample are slightly tapered with thinner sections near the tip. The growth of these wires during cooling is surprising, since thermodynamic considerations based on the various binary phase diagrams[3-5] indicate that a simple phase-separated microstructure should form upon cooling.

We have carried out additional experiments to understand the conditions that lead to wire growth. For Au, Ag, and In, temperatures of at least ~225 °C were required for at least two hours for wires to form. Heating for longer durations and at higher temperatures (up to 320 °C) resulted in more uniform coverage of wires on sample surfaces. Other metal foils (Sn and Cu) were also tested under similar conditions, but heating these metals with Li did not result in the growth of wires despite repeated tests at different temperatures. For the materials that did grow wires, optical microscopy experiments in a glove box have revealed that the wires grow during the cooling process (not the heating step). A microscope in a glove box was used to image a Li-Au sample during heating and cooling. Upon heating, the sample (with Au foil initially on top of the Li foil) changed from a metallic gold color to a dark gray color, indicating the formation of a Li-Au alloy. The sample was then removed from the hot plate to induce rapid cooling over a few minutes; during this process, the majority of the surface of the sample turned bright red, as shown by the optical images in Fig. 3. SEM images of the same sample after this process revealed that the red portions contained a high concentration of wires, while dull gray portions did not. The red color likely arises from the wire regions because of optical effects due to the small diameters of the wires.[6]

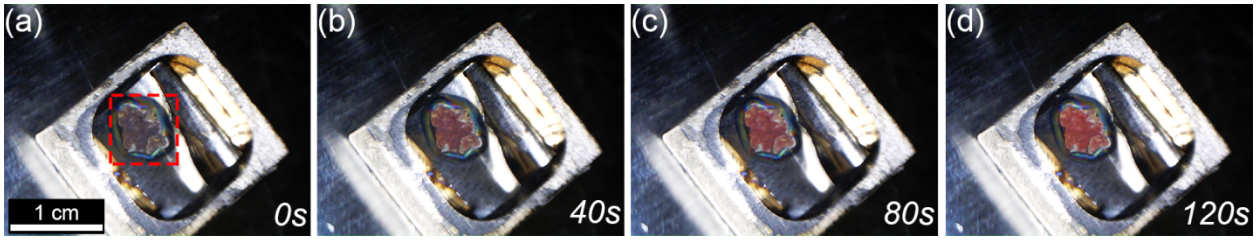

Figure 3. Optical images taken within a glove box of a Li-Au sample during cooling for **(a)** 0 s, **(b)** 40 s, **(c)** 80 s, and **(d)** 120 s. The emergence of the red color during cooling signifies the growth of wires.

Figure 4a-c show an SEM image and EDS maps of two wires grown from a Li-Au sample. As shown in Fig. 4b, only the tips of the wires contain Au, while both the tip and the length of the wires contain the element O (Fig. 4c). Unfortunately, Li cannot be detected with EDS due to its low atomic number. X-ray diffraction (XRD) has also been used to investigate the crystal structure of wire samples. To prevent significant oxidation from exposure to atmosphere, the prepared samples were covered with mylar films inside the glove box, which gives rise to broad diffraction intensity at low 2θ regions. The XRD spectrum of a Li-Au wire sample in Fig. 4d shows that the material is primarily the cubic $Li_{15}Au_4$ alloy phase. In addition, Li_3Au peaks with weaker intensities were observed in the spectrum. Low-intensity peaks from Li_2O were also present.

Notably, diffraction peaks from Li or Au were not detected, even though these were the primary peaks detected in pristine Li-Au bilayers before heating. Although XRD studies provided some insight regarding the phase transformations in these samples, it is unclear from the XRD alone whether the wires are made of $Li_{15}Au_4$ alloy or some other material since the entire underlying sample likely contributes to the diffraction spectrum, and the wires only covered the surface.

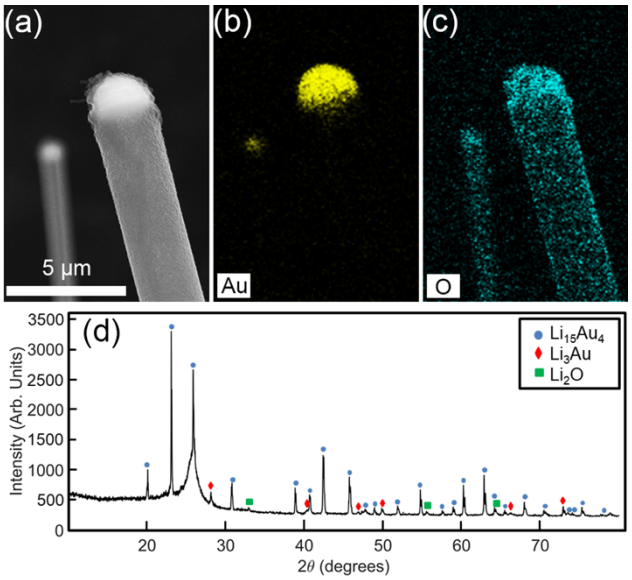

Figure 4. (a) SEM image of the tips of two wires grown from Li-Au bilayer samples (6:1 molar ratio). **(b)** X-ray energy dispersive spectroscopy (EDS) map of the image in (a) showing the presence of Au in the wire tips but not in the shafts of the wires. **(c)** EDS map showing the element O within the wires. **(d)** XRD spectrum of a Li-Au wire sample.

To examine the structure of the wires in more detail, transmission electron microscopy (TEM) and selected area electron diffraction (SAED) were used. Cryo-TEM using liquid nitrogen was found to be necessary to stabilize the wires when imaging in a 300 kV TEM. A cryo TEM image of a wire exposed to atmosphere for ~30 s during transfer into the instrument is shown in Fig. 5a. As shown by the magnified view in Fig. 5b, this wire has an Au-rich tip (the darker region) which is sheathed by lighter material. The lower section of the wire has a hollow or porous center with lighter contrast (Fig. 5c). SAED patterns of the tip and of the shaft (Fig. 5d and e) show that the wire is made of polycrystalline LiOH, and the contrast in the image indicates small grain sizes on the order of tens of nm. Finally, the seemingly hollow structure of the shaft of the wire is notable; such structures were repeatedly observed with SEM and TEM (although wires were not always hollow). Taken together, these results show that the wires are made up of LiOH with Au-rich tips, and the data further suggest that the wires convert to polycrystalline LiOH after initially growing as Li metal. Li metal wires could be converted to LiOH during growth due to low concentrations (~0.1-2 ppm) of O_2 and H_2O in the glove box. The observed hollow shafts strongly suggest such a conversion process, since Li would diffuse radially outward to react with moisture at the surface in a manner akin to the Kirkendall effect.[7] We note that LiOH was not detected in the XRD studies, which is likely because the LiOH grains were too small to produce significant diffraction intensity. Furthermore, the Au-containing $Li_{15}Au_4$ alloy should diffract more strongly than Li or LiOH because of the much higher mass absorption coefficient of Au. The XRD results likely mostly detect the bulk $Li_{15}Au_4$ alloy that is beneath the wires, as most of the Au used during the synthesis remained below the wires and did not participate in wire growth.

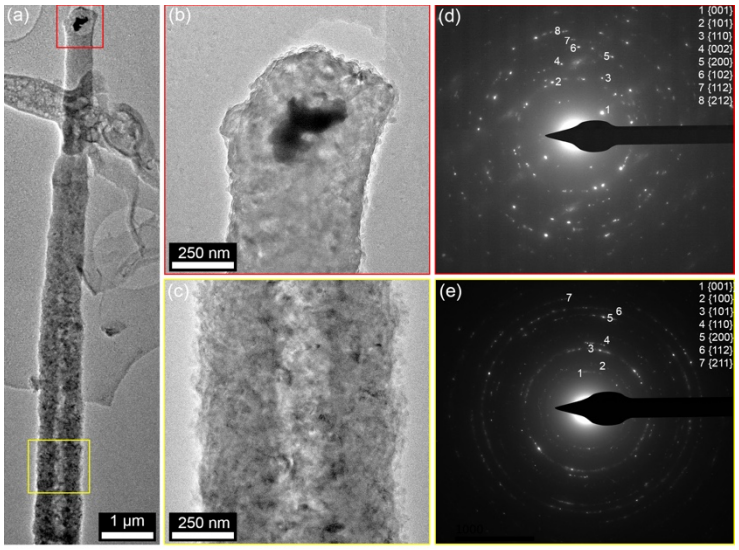

Figure 5. (a) Cryo-TEM image of a wire grown from a Li-Au sample (Li:Au molar ratio of 20:1) after transfer through atmosphere. The colored boxes correspond to the locations of the magnified images in (b, c). **(b)** A magnified image of the tip of the wire. **(c)** A magnified image of the shaft of the wire. **(d, e)** SAED patterns of the tip and the shaft, respectively, show the presence of polycrystalline LiOH.

These observations have led us to postulate a mechanism for wire growth in which Li metal wires grow from Li-Au alloy seed particles in a related fashion to VLS growth of semiconductor nanowires. Figure 6 shows schematics of the proposed wire growth process, as well as the Li-rich portion of the Li-Au binary phase diagram.[5] Upon cooling Li-rich liquid alloys from ~300 °C, the bulk liquid alloy begins to decrease in temperature along the red line in Fig. 6e until the two-phase region separating the solid Li phase and the liquid alloy phase is reached at point (b) in the phase diagram. At this point, solid Li metal (with a small amount of dissolved Au) nucleates from the liquid alloy phase, and based on our observations, it is likely that this growth occurs from

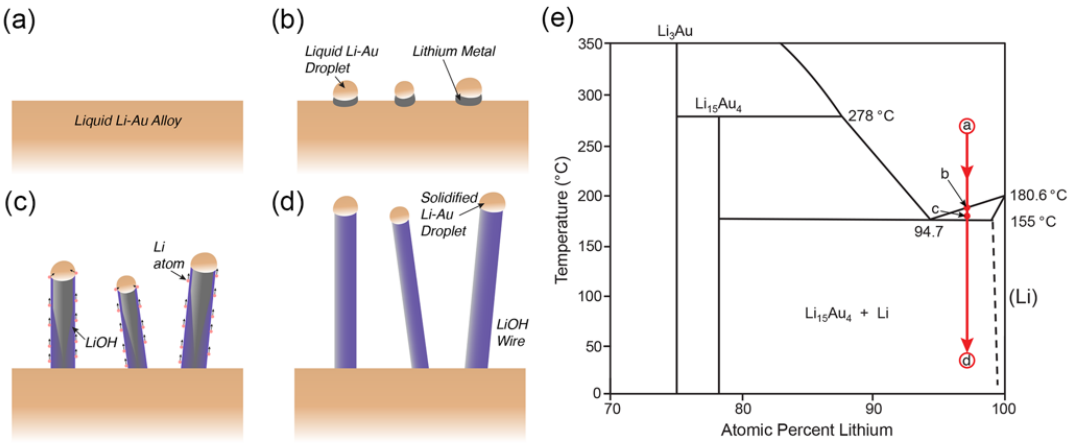

Figure 6. (a-d) Schematics showing the postulated growth mechanism. **(e)** The Li-rich region of the Li-Au phase diagram.

individual liquid alloy catalyst droplets, as shown in Fig. 6b. These Li metal crystals continue to grow as the sample is further cooled through the two-phase region (Fig. 6c), and these wires push up the liquid Li-Au droplets as they grow. A critical aspect of this growth mode is that additional Li atoms must continually enter and alloy with the droplet at the tip instead of directly attaching to the sidewalls of the Li wires. We postulate that the formation of passivating LiOH plays a key role in this step. If LiOH forms on the surface of the Li wires as growth occurs, as shown in Fig. 6c, it could cause Li atoms diffusing from the underlying liquid alloy reservoir to diffuse along the surface of the wires to dissolve in the tips of the wires instead of directly attaching to the solid Li. Recent work has shown the importance of surface passivation in catalyzed nanowire growth,[2] and we predict that passivation plays a key role here.

To summarize this section, we have demonstrated a new, simple, low-temperature method for the fabrication of nanowires and microwires via the cooling of liquid Li-metal alloys that are rich in Li. While the wires consist of LiOH and are not metallic, the evidence described above suggests that they grow as Li metal wires and are converted to LiOH during and/or after growth. If this is the case, this would indicate that it is possible to grow metallic nanowires (perhaps with metals other than lithium) with vapor-liquid-solid-like mechanisms. This represents a new method for using alloying to make nanostructures.

IIIb. Development of new procedures to create monolithic porous metals via lithium dealloying

Selective dealloying of binary alloys containing noble metals, such as Ag-Au or Cu-Au, has been extensively studied to create porous structures. These materials can form a bicontinuous ligament morphology with uniform size of ligaments less than a few hundred nanometers upon (electro)chemical dealloying of the more reactive element. However, conventional dealloying methods are only useful for creating porous noble metals due to the chemistries utilized. Here, we develop new dealloying procedures capable of creating monolithic porous metals in a wider variety of chemistries than currently possible.

Porous In or Sn structures were fabricated by dealloying Li from Li-In or Li-Sn alloys. Before dealloying, Li-In or Li-Sn alloys were created in an Ar-filled glovebox with H_2O and O_2 levels <2.0 ppm. In or Sn microparticles are compressed at 250 MPa into a thin pellet using a hydraulic press. The surface contamination layer of Li metal is physically removed. A thin pellet of In or Sn is pressed with the cleaned Li metal in the glovebox. A molar ratio of 5:1 (Li:M, where M = In or Sn) is used for alloying. The sample was heated in a stainless steel heating holder on a hot plate within the glovebox at 220-230 °C for 4 h. After alloying, Li-In or Li-Sn alloys were chemically dealloyed by first immersing in anhydrous methanol inside glovebox and placed on a hot plate outside the glove box at 60 °C for 8 h to facilitate dealloying. The sample was then rinsed with clean anhydrous methanol 3 times in the fume hood. Other experiments were carried out by varying the molar ratio and dealloying conditions such as temperature and time. Figure 7 shows

the schematic of the fabrication process. This synthesis reproducibly created the porous foils as shown in the scanning electron microscopy (SEM) images in Figure 7b and c.

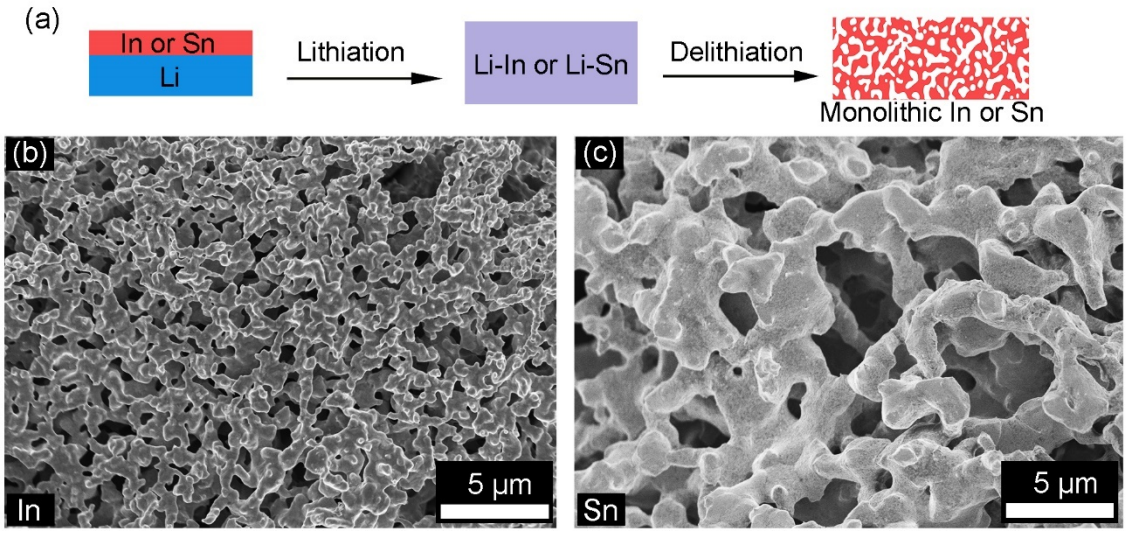

Figure 7. Synthesis and characterization of porous metals by chemical dealloying of Li. (a) Schematic showing the synthesis of porous In or Sn foil via the delloying of a Li-In or Li-Sn alloy (a Li:In or Li:Sn molar ratio of 5:1 was used). **(b)** SEM image of a dealloyed In sample. **(c)** SEM image of a dealloyed Sn sample.

The dealloying of Li-rich alloys with other metals, such as Bi, Sb, Ag, and Au, was also investigated, but these materials did not form a porous morphology like In or Sn under these conditions (shown in Figure 8). Au and Ag showed cracks after delithiation, and Sb was pulverized to form smaller particles. Bi retained its bulk foil form with embedded porosity. These findings suggest that different reaction and lithium diffusion kinetics within these alloys could play an important role in determining the final morphology. Porous ligamentary structures were observed at least partially for Li:In molar ratios greater than 2:1. In addition, further experiments with dealloying time as a variable showed that porous structures form after dealloying for at least 2 h at 60 °C. After 6 h, ligaments with improved uniformity were observed, which could be due to the continued diffusion of Li out of the monolith. Dealloying for 48 h did not significantly change the ligament morphology.

These porous metals created via dealloying of Li are consistent with a handful of previous studies on using Li as a processing agent. Dealloying of Li from Li-Al alloy particles has resulted in the formation of Al alkoxide nanowires due to the reaction of Al with ethanol.[12] In our case, both Sn and In were observed to form porous metallic structures rather than oxides, which is likely due to the reduced tendency of these metals to oxidize compared to Al. In addition, Li-rich Li-Sn particles have been shown to form porous morphologies during electrochemical dealloying at high currents.[38] This study found that a fast dealloying rate was important for forming porous, bicontinuous structures. This is because the Li dissolution rate has to be fast enough to minimize surface diffusion smoothening, which causes Li redistribution that can prevent pore formation. For

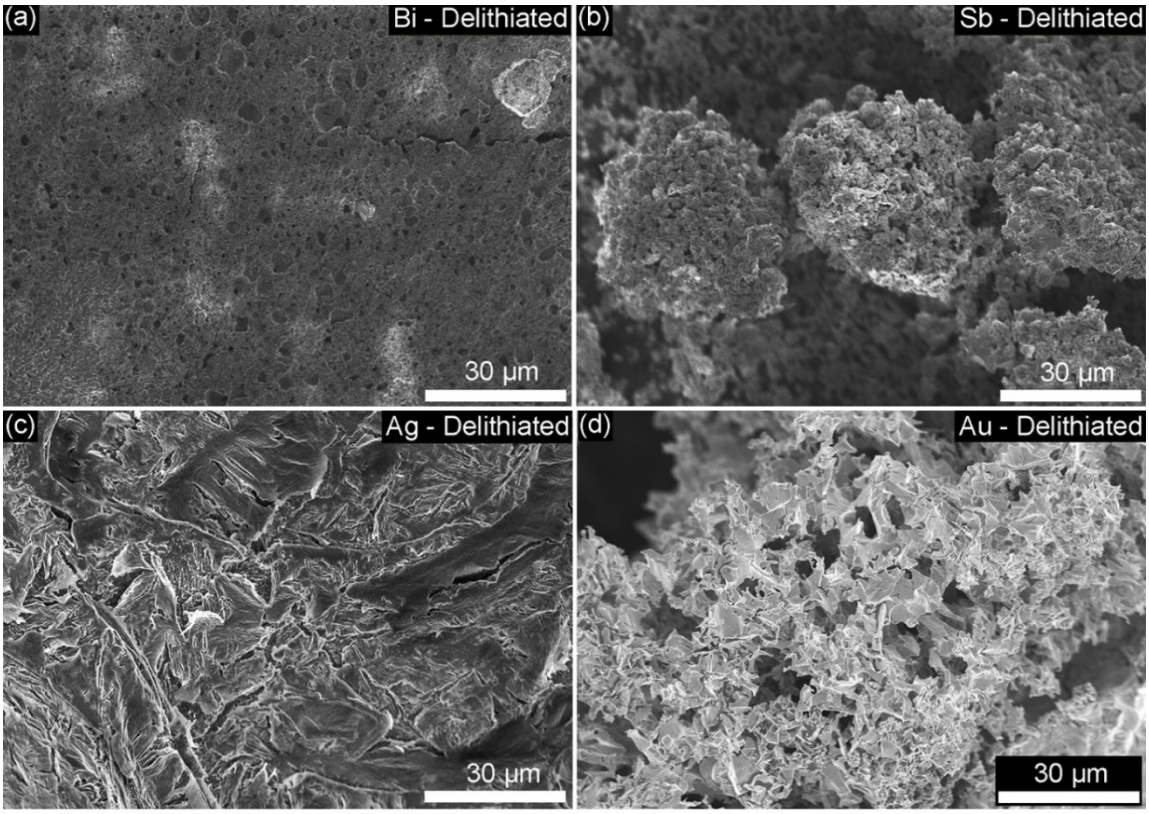

Figure 8. SEM images of dealloyed Li-M samples (M = Bi, Sb, Ag, or Au) with a Li:M molar ratio of 5:1 heated for 4 hours at 220 °C and delithiated with dry methanol for 8 hours at 60 °C. Bi and Sb microparticles were pressed to make a pellet for lithiation. Ag and Au foils were directly lithiated and dealloyed. **(a)** Bi **(b)** Sb, **(c)** Ag, **(d)** Au. Different dealloyed morphologies were observed in each case.

comparison with chemical dealloying, we performed electrochemical dealloying experiments. In these experiments, In pellets were electrochemically lithiated and delithiated in coin cells at current densities ranging from 0.3 to 2.0 mA cm^{-2}. Electrochemical delithiation of the Li-In alloy did not result in a porous structure as observed from chemically dealloying; this difference in morphologies is likely a result of the lower dealloying rates that must be used in electrochemical Li removal. Importantly, the relatively large mass of the metal pellet (~2 mg) will likely make it impossible to sustain a high enough electrochemical dealloying rate for the formation of bicontinuous porosity in the full pellet, and thus the free-corrosion dealloying is essential for creating the porous structure.

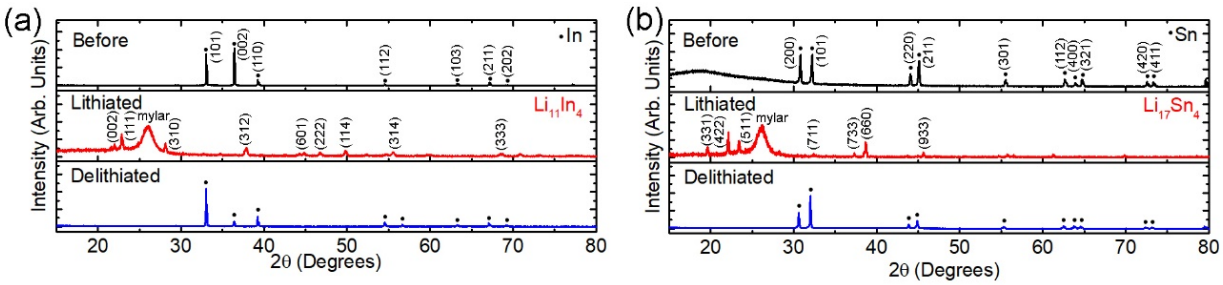

Figure 9. XRD patterns of In **(a)** and Sn **(b)** samples at different steps of the synthetic procedure.

Structural characterization of dealloyed materials. The In and Sn samples exhibited consistent ligament size across the entire area of the samples. The averaged width of the ligaments from SEM images was measured to be 700 ± 210 nm for In and 1.80 ± 0.37 μm for Sn. X-ray diffraction (XRD) was used to investigate the phase evolution during the synthetic procedure shown in Figure 9. XRD of the pristine In and Sn samples before alloying showed the expected tetragonal crystal structures. After chemical alloying, the detected phases are primarily $Li_{11}In_4$ (ICDD 04-021-2444) and $Li_{17}Sn_4$ (ICDD 04-014-6237). Li_2O or Li peaks were not detected. The broad peaks from 25° to 30° is from the mylar film used to protect the lithiated samples from oxidation during XRD measurements. After removing Li by soaking the samples in the dry methanol, the materials returned to the original metallic phases. The change in peak intensities is

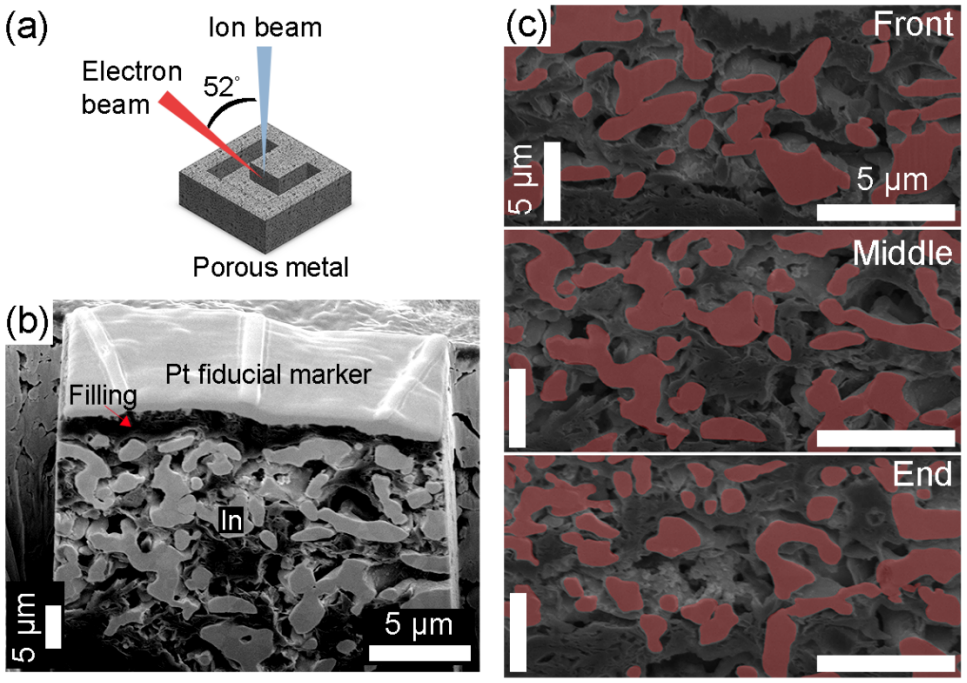

Figure 10. Physical characterization of the porous In. (a) Schematic showing the FIB tomography experiment and trench geometry used for this measurement. **(b)** An SEM image of the front surface of the milled porous In sample with carbon infill. **(c)** Segmented SEM images of the front, middle, and end slices of the milled volume, in which the artificial red overlay is the segmented metallic phase.

attributed to microstructural changes during the transformation from a dense pellet to a porous structure. After dealloying, no Li or Li_2O was detected; this indicates that the Li was completely removed from the Li alloys after delithiation.

The porosity and ligament structures were further analyzed using focused ion beam (FIB) tomography. Figure 10 shows a schematic of the FIB tomography experiment. Figure 10b shows a single image from the experiment and Figure 10c shows image slices from different depths, along with the segmented metallic regions overlaid in red. The full 3D reconstruction of the metallic phase within a ~3307 μm^3 volume is shown in Figure 11. Within this 3307 μm^3 total volume, the measured internal volume of In metal was 1055 μm^3, and the surface area was 3903 μm^2. This value of surface area is 2.9 times that of a dense metal foil. The pore volume of the material was 68% of the total volume. In addition, we characterized the pore tortuosity of the segmented volume using Dragonfly software. Tortuosity quantitatively describes transport pathways through a given phase, and it is defined as $\tau = L_{eff}/L$, where L_{eff} is the length of a curvilinear path through a structure and L is the Euclidean distance through the structure.[113,114] A tortuosity of 1.60 was measured for the segmented volume in Figure 11.

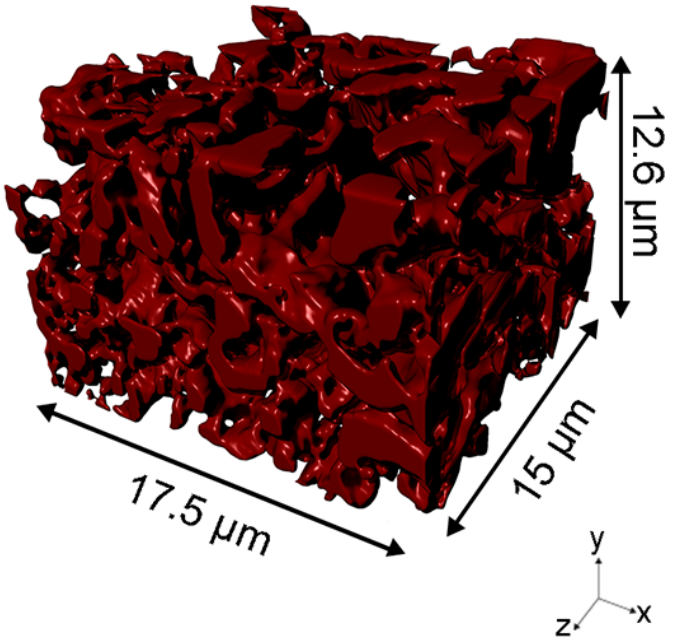

Figure 11. Full 3D tomographic reconstruction of the porous In sample.

IIIc. Investigation of lithium storage properties of porous metals

We next investigated the porous metal foils described in the prior section as battery electrodes in both solid-state and liquid-state electrolyte systems. We found that the porous material exhibits higher specific capacity, better cycle life and rate capability than dense foils within solid-state batteries. Our results show that porous metal anodes could enable high capacity

and extended cycle life within solid-state batteries, which could be important for structural battery applications.

Porous In electrodes were investigated as anodes for solid-state batteries (SSBs). Solid-state battery cells with a Li counter electrode were made using a custom cell assembly inside an Ar-filled glove box. $Li_{10}SnP_2S_{12}$ (LSPS) was used as the solid-state electrolyte (SSE). Figure 12a shows cross-sectional SEM images of porous electrodes after being pressed into the battery before cycling. Porous ligaments were preserved after being pressed at 15 MPa within the solid-state cell assembly. Additional SEM images of the porous In electrode after being pressed in the solid-state battery assembly are shown in Figure 13. Figure 12b shows the first discharge and charge of a porous electrode compared to a cell with a dense foil working electrode with a similar mass loading. The porous electrode had a specific capacity of 350 mAh g^{-1}, while the foil had a specific capacity of 270 mAh g^{-1} for the first discharge; thus, the porous electrode showed ~1.3 times higher specific capacity than the dense foil.

The rate behavior and long-term cycling performance of these structures were tested. The rate behavior of the electrode materials was examined at various rates from C/30 to C/10 (i.e., 30

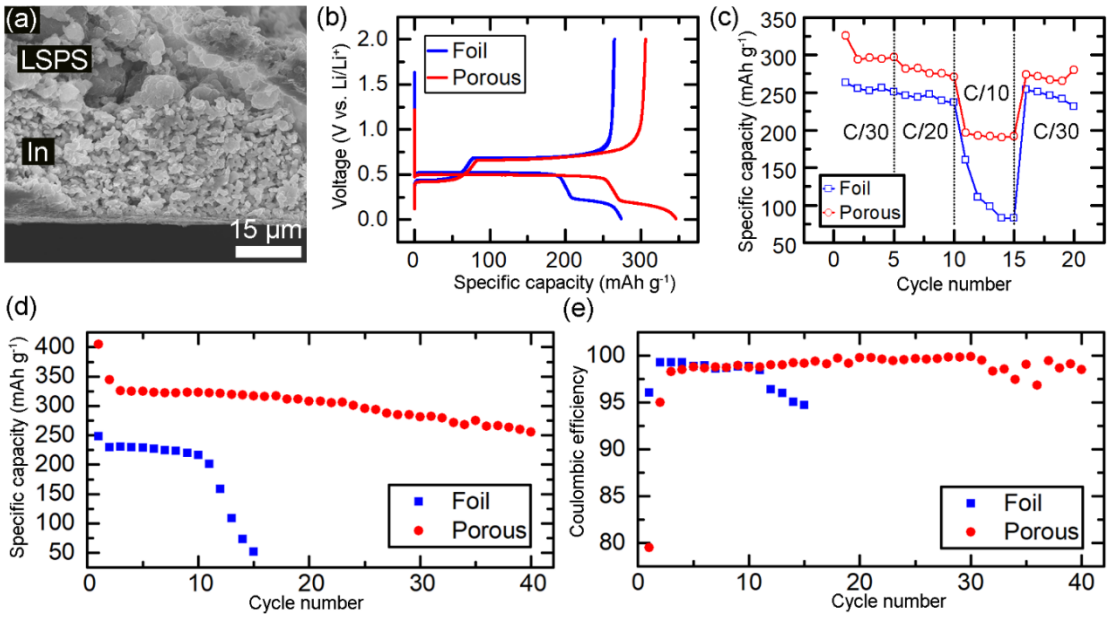

Figure 12. Porous In electrodes within solid-state batteries. (a) Cross-sectional SEM image of a porous In electrode that was pressed within a solid-state cell and removed for imaging. **(b)** First galvanostatic lithiation/delithiation of a porous In sample and a dense In foil sample. The current density was 0.60 mA cm^{-2} for the dense foil and 0.69 mA cm^{-2} for the porous electrode. Both electrodes had mass loadings between 1 and 2 mg, and lithium foil was used as the counter electrode. **(c)** Rate capability of a porous In electrode and a dense In foil electrode within solid-state cells at various rates from C/30 to C/10 (1C = 1012 mA g^{-1} of In). Lithium foil was used as the counter electrode. **(d)** Capacity retention with cycling for a porous electrode and a dense foil electrode at a rate of C/20 (0.75 mA cm^{-2}). For long-term stability, these cells included a thick In metal foil in contact with the Li counter electrode to reduce interfacial degradation of the SSE (see methods). **(e)** Coulombic efficiency from the cells in (d).

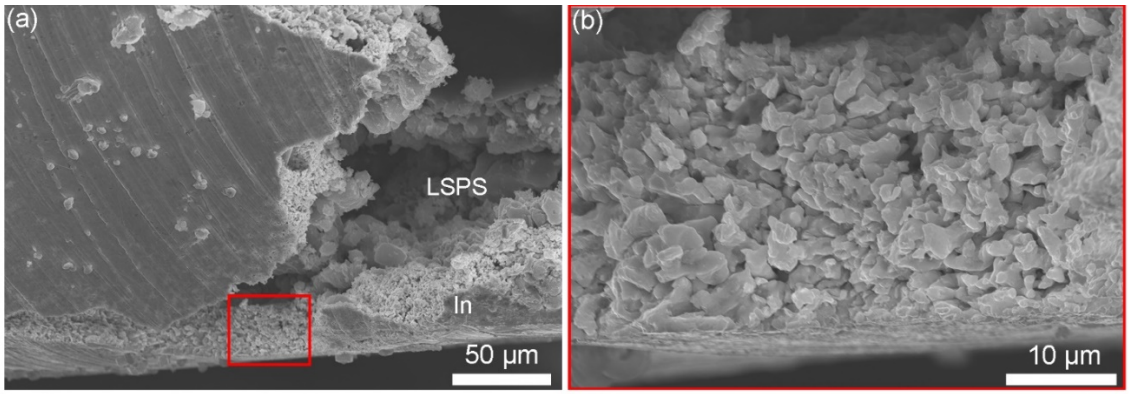

Figure 13. SEM images of a porous In electrode after being pressed in the solid-state battery assembly at 15 MPa. The In electrode was intentionally fractured to expose the cross section for imaging. **(a)** A low-magnification SEM image of the pristine porous electrode. The image shows that the bottom surface is flat and smooth. The red box in the image corresponds to the magnified area imaged in (b). **(b)** Magnified SEM image of the cross-section of the porous In electrode showing that the connected ligaments are present.

h for total discharge and 10 h for total discharge). At all currents, porous In electrodes exhibit higher capacity than the dense foil (Fig. 12c). In addition, Figure 12d shows the capacity retention with cycling for a porous In electrode vs. a dense foil electrode over 40 cycles. The higher first-discharge specific capacity of 408 mAh g^{-1} was achieved for the porous material compared to the dense foil (250 mAh g^{-1}). The porous electrode also featured better capacity retention (a decrease from 408 mAh g^{-1} to 300 mAh g^{-1} over 40 cycles) compared to the dense foil, which experienced steep capacity decay after 10 cycles. Figure 12e shows the Coulombic efficiency (CE) of the porous electrode and dense foil. The dense In foil featured an initial CE of 94.0% with an average value of 97.7% over 15 cycles, but the CE of the porous electrode increased from 80.0% in the initial cycle to an average value of 98.5% over 50 cycles. In these longer-term cycling tests, the counter electrodes consisted of a 50 μm thick In foil placed at the interface between the SSE and the Li metal to improve chemical stability of the SSE during cycling,[99] which limited SSE degradation and provided a better indication of the electrochemical stability of the In working electrodes themselves. Finally, we note that the higher observed capacity and better cycle life of the porous In material was observed consistently over multiple cells. The improved capacity and cycle life of the porous metal electrodes is likely due to the capability of the porous material to accommodate the volume changes during lithiation/delithiation while minimizing mechanical damage of the cell stack and retaining electron transport pathways.

We also examined the electrochemical behavior of the porous electrodes in conventional liquid-electrolyte cells. Half cells were used with Li as the counter electrode, and we compared the electrochemical behavior of porous electrodes with dense foil. We utilized a carbonate-based electrolyte with a mixture of ethyl methyl carbonate (EMC), ethylene carbonate (EC), fluoroethylene carbonate (FEC), and $LiPF_6$ salt. Figures 14a and b show galvanostatic tests over 15 cycles for dense In foil and porous electrodes, respectively. These data show that the porous

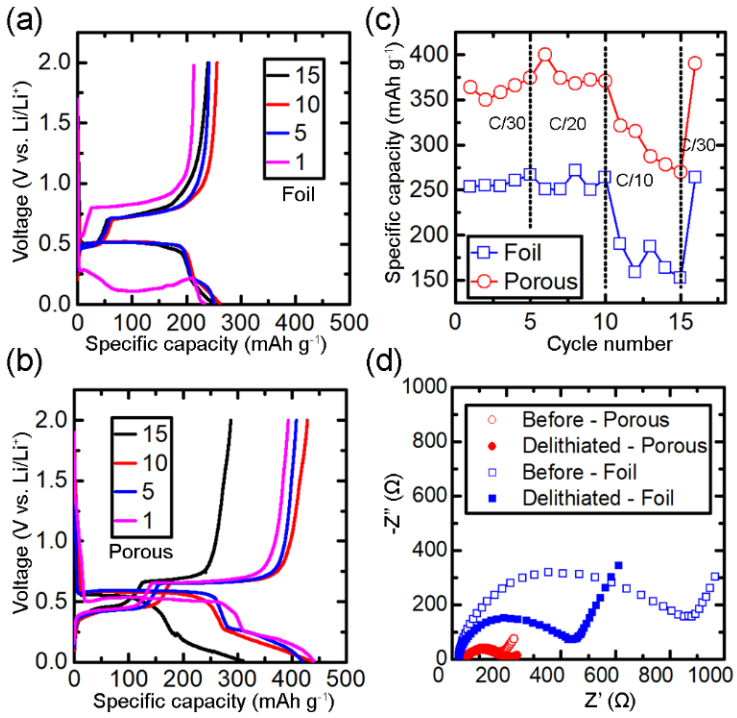

Figure 14. Porous In electrodes within liquid-cell batteries. (a, b) The first (pink), fifth (blue), 10th (red), and 15th (black) discharge/charge curves from half-cells with dense In foil (a) or porous In foil (b) working electrodes tested at C/20 (current density of 0.65 mA cm^{-2}). **(c)** Rate capability of porous In and dense In foil within half cells at various rates from C/30 to C/10 (1C = 1012 mA g^{-1} of In). **(d)** Nyquist plots showing the impedance spectra before and after one discharge/charge cycle for each type of electrode.

electrode exhibits higher specific capacity than the dense foil. During the first lithiation of the dense foil, the electrode potential was depressed below the expected plateau of 0.5 V vs. Li/Li$^+$. The first lithiation of the porous electrode did not feature this lowered voltage, and it was also not observed in the solid-state testing of the dense In foil with similar mass loadings. The lowered initial discharge potential in Figure 14a may be due to a combination of a lower surface area of the dense foil compared to the porous sample and higher charge transfer resistance in the liquid compared to the solid. From the first to the 10th cycle, the specific capacity of the dense foil had an average value of 247 mAh g^{-1} (Figure 14a), while the porous electrode had a higher average specific capacity of 432 mAh g^{-1} (Figure 14b). Rate sensitivity tests were performed for both types of electrodes in the liquid electrolyte, as shown in Figure 14c. These experiments showed that porous electrodes exhibited higher specific capacity across the range of rates from C/30 to C/10, which is a similar result to the solid-state case. Figure 14d shows electrochemical impedance spectroscopy results. The charge transfer resistance before cycling for the porous In electrode was 265 Ω, which is lower than the value of 880 Ω for the dense In foil. This is likely due to the increased surface area of the porous material, and the surface area ratio of 2.9 measured with FIB tomography correlates well with these different charge transfer resistance values. After one cycle,

the charge transfer resistance decreased to 147 Ω and 444 Ω for the porous and dense foil electrodes, respectively. This decrease could be due to a stable SEI formed on the surface of the electrodes.

The specific capacity attained using the porous In electrodes was superior to that of dense In foil in both solid-state and liquid-electrolyte cells. Furthermore, the porous electrodes showed long cycle life in solid-state cells but failed faster in the liquid cells than dense In foil. After the ~15th cycle in liquid cells, capacity decay was severe for the porous electrodes. This is likely due to the continuous growth of SEI on the higher surface area of the porous electrodes, which can eventually impede ion transport. In solid-state cells, the higher surface area of the porous material enables improved accommodation of volume changes, while the interface with the SSE is confined to only a small portion of the porous material. Thus, an SEI does not grow to cover the entire surface area of the porous In, but instead only covers a planar interface. The bulk and surface of the porous In materials allow for Li diffusion at a rate that is fast enough to support the currents used herein, and a liquid electrolyte is thus not needed to infiltrate the structure. This advantageous geometry improves cycling stability while also allowing for high capacity.

IIId. In situ TEM of reaction-induced sintering. Throughout this project we observed the effects of "reaction induced sintering," where Li-rich alloy particles spontaneously join together. We also made an effort to characterize this process with *in situ* transmission electron microscopy, with moderate success. In these experiments, a specialized probing-biasing sample holder was used within the TEM to physically bring a piece of lithium (coated with Li_2O) into contact with Sn nanoparticles. A bias was then applied to drive Li^+ through the Li_2O surface coating to react with the Sn, and upon reversal of the bias, the Li is removed. Figure 15a shows the experimental setup with the Li in the bottom of the frame and the Sn particles coating a tungsten rod in the upper part of the frame. The Sn particles have a fairly uniform size distribution (~25 nm in diameter), and they are each coated with a 3-5 nm thick surface oxide layer (Fig. 15b). The selected-area electron diffraction (SAED) pattern of the Sn particles in Fig. 15b showed that they take the expected tetragonal phase. The particles undergo expansion during lithiation and contraction during delithiation, leaving behind the deformed particles in Fig. 15c. The oxide layer is still visible on these particles, but the particles have not undergone significant sintering or merging. The oxide layer likely prevented sintering or joining between the particles.

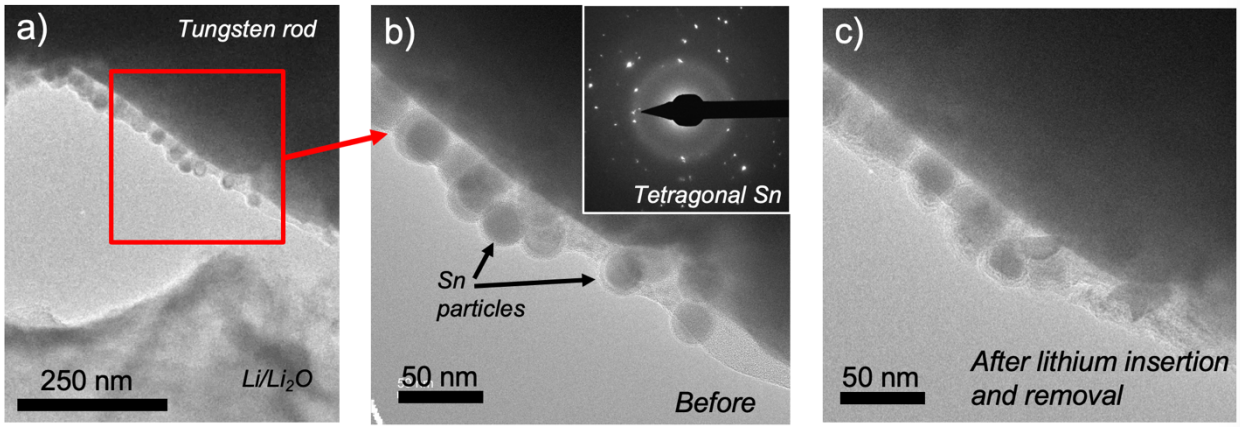

Figure 15. *In situ* TEM of the reaction of Sn nanoparticles with lithium. **a)** Experimental setup showing the piece of Li at the bottom of the frame and the tungsten rod at the top of the frame. The Sn particles coat the tungsten rod. **b)** Magnified view of the pristine Sn particles coating the tungsten rod. The spherical particles have a thin oxide coating. The SAED pattern shows that the particles take the tetragonal Sn phase. **c)** The same particles after lithiation and delithiation. The particles are damaged and deformed, and sintering has likely been largely prevented by the still-visible oxide layers.

IIIe. Stress measurement during alloying transformations

In the last few months of the project, the project team worked on developing and implementing a force measurement system within solid-state electrochemical cells to measure how the stress within alloy metals evolves during electrochemical insertion and removal of lithium. These measurements are designed to provide insight into the evolution of the metal morphology during reactions, as well as during the synthesis of the porous metals. The project team has constructed a "pressure cell" that allows for uniaxial compression, real-time force measurement, and simultaneous electrochemical testing of solid-state electrochemical cells (Fig. 16). This cell allows for battery materials to be loaded and compressed with the plungers to a specific uniaxial stress determined by the torque applied to the top bolts. A force sensor is integrated into the bottom of the cell and can sensitively measure both the applied stress and changes in stress due to volume changes during lithium alloying with the active metal. The output of the force sensor was wired through a signal conditioner and custom Arduino setup to digitize and record the data. This setup is expected to be useful to understand the chemo-mechanics of alloying reactions, and it was as an important aspect of Specific Research Objective 3 of this project.

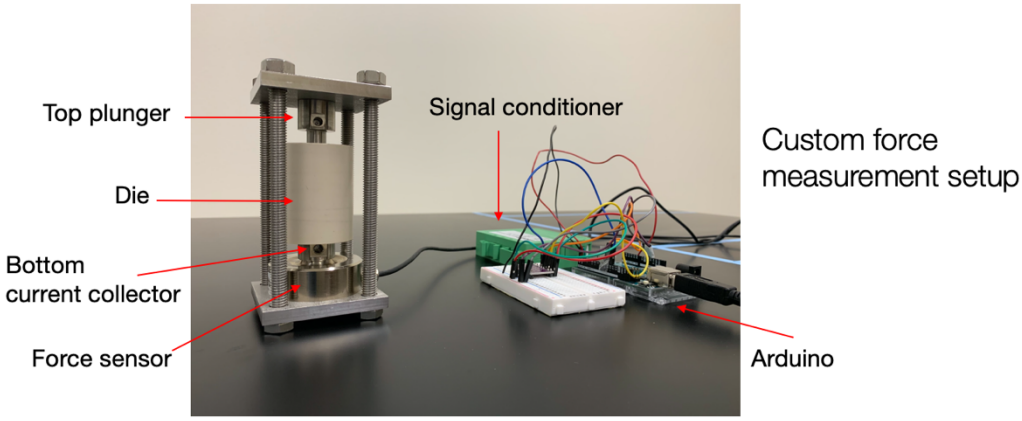

Figure 16. Photograph of custom force sensor compression cell constructed for simultaneous application of uniaxial stress, measurement of force, and electrochemical testing.

During this project, the project team used this setup to measure the stress evolution of a solid-state battery with lithium metal electrodes in support of another project focused on solid-state battery materials. The data are shown in Fig. 17. Finally, although our project has ended, the lead GRA has continued using this setup to measure stress evolution during alloying/dealloying of lithium metal alloys.

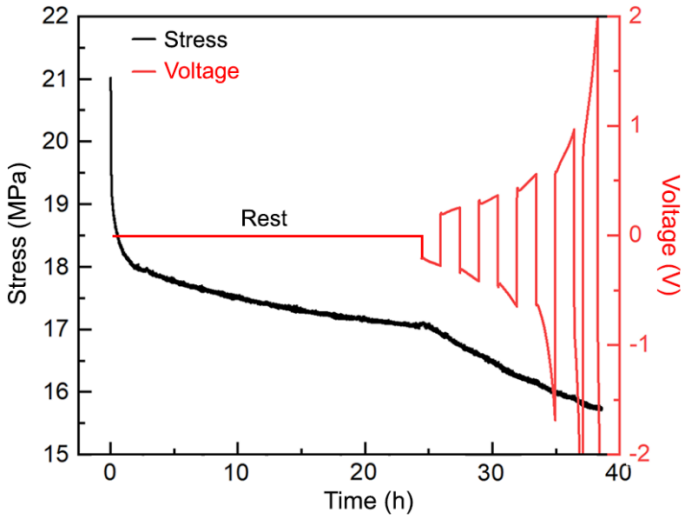

Figure 17. The stack pressure (black line) measured using a force sensor during *ex situ* cycling of a lithium symmetric cell at 1 mA cm^{-2} (voltage curve shown in red line) using $Li_{10}SnP_2S_{12}$ solid-state electrolyte. After assembly, the cell rested for 24 h before operation. Over the first hour, the stack pressure sharply decreased, which is likely due to flow of the lithium metal electrodes. Over the remainder of the first 24 h, the stack pressure decreased more gradually due to the chemical reaction between Li and LSPS. Once cycling began, the rate of pressure loss increased, as shown by the steeper slope in the pressure curve. This can be explained by the increased rate of solid electrolyte decomposition and interphase formation during cycling.

References

1 Weissmüller, J., Newman, R. C., Jin, H.-J., Hodge, A. M. & Kysar, J. W. Nanoporous Metals by Alloy Corrosion: Formation and Mechanical Properties *MRS Bulletin* **34**, 577-586 (2009).

2 Ek, M. & Filler, M. A. Atomic-Scale Choreography of Vapor–Liquid–Solid Nanowire Growth. *Accounts of Chemical Research* **51**, 118-126, doi:10.1021/acs.accounts.7b00392 (2018).

3 Sangster, J. & Pelton, A. D. The In-Li System. *Journal of Phase Equilibria and Diffusion* **12**, 290-292 (1991).

4 Pelton, A. D. The Ag-Li (Silver-Lithium) System. *Bulletin of Alloy Phase Diagrams* **7**, 223-228 (1986).

5 Pelton, A. D. The Au-Li System. *Bulletin of Alloy Phase Diagrams* **7**, 228-231 (1986).

6 Dhindsa, N. Adjustable optical response of amorphous silicon nanowires integrated with thin films. *Nanotechnology* **27** (2016).

7 Wang, W., Dahl, M. & Yin, Y. Hollow nanocrystals through the nanoscale Kirkendall effect. *Chemistry of Materials* **25**, 1179-1189 (2013).